

Gas-Phase Peroxyl Radical Recombination Reactions: A Computational Study of Formation and Decomposition of Tetroxides

Published as part of *The Journal of Physical Chemistry virtual special issue "Advances in Atmospheric Chemical and Physical Processes"*.

Vili-Taneli Salo,* Rashid Valiev, Susi Lehtola, and Theo Kurtén*



Cite This: *J. Phys. Chem. A* 2022, 126, 4046–4056



Read Online

ACCESS |



Metrics & More

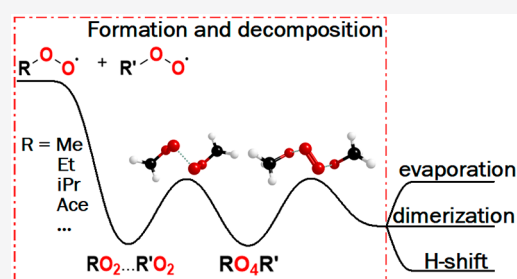


Article Recommendations



Supporting Information

ABSTRACT: The recombination (“dimerization”) of peroxy radicals ($\text{RO}_2\bullet$) is one of the pathways suggested in the literature for the formation of peroxides (ROOR' , often referred to as dimers or accretion products in the literature) in the atmosphere. It is generally accepted that these dimers play a major role in the first steps of the formation of submicron aerosol particles. However, the precise reaction pathways and energetics of $\text{RO}_2\bullet + \text{R}'\text{O}_2\bullet$ reactions are still unknown. In this work, we have studied the formation of tetroxide intermediates ($\text{RO}_4\text{R}'$): their formation from two peroxy radicals and their decomposition to triplet molecular oxygen ($^3\text{O}_2$) and a triplet pair of alkoxy radicals ($\text{RO}\bullet$). We demonstrate this mechanism for several atmospherically relevant primary and secondary peroxy radicals. The potential energy surface corresponds to an overall singlet state. The subsequent reaction channels of the alkoxy radicals include, but are not limited to, their dimerization into ROOR' . Our work considers the multiconfigurational character of the tetroxides and the intermediate phases of the reaction, leading to reliable mechanistic insights for the formation and decomposition of the tetroxides. Despite substantial uncertainties in the computed energetics, our results demonstrate that the barrier heights along the reaction path are invariably small for these systems. This suggests that the reaction mechanism, previously validated at a multireference level only for methyl peroxy radicals, is a plausible pathway for the formation of aerosol-relevant larger peroxides in the atmosphere.



1. INTRODUCTION

Peroxy radicals are primary intermediates in the oxidation of volatile organic compounds (VOC), such as hydrocarbons, in the atmosphere.^{1,2} These compounds and their downstream oxidation and aggregation products play an essential role in the formation of tropospheric secondary organic aerosols (SOA).^{3,4} Not only do tropospheric aerosols and other fine particulate matter pose severe respiratory and cardiovascular health risks in polluted urban areas,^{5,6} but they also modulate climate on a global scale.⁷

Hydrocarbons are emitted into the atmosphere via both anthropogenic and biogenic processes.^{8,9} The main emitted hydrocarbons include methane, ethane, other volatile higher alkanes, alkenes, alkynes, ketones, aldehydes, etc. Simple aliphatics, aromatics, and alkenes are mainly of anthropogenic origin; sources include incomplete fossil fuel burning, leaking or evaporation of volatile organic compounds in industrial processes, and human-controlled biological processes.⁹ Biogenic hydrocarbon emissions can be divided into two subcategories: emissions due to microbial activity and emissions of biosynthetic VOCs by higher plants. The bulk of the biogenic emissions are composed of methane from

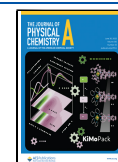
microbial methanogenesis,¹⁰ and of isoprene and other volatile terpenes and terpenoids from plants.¹¹ The biogenic C_{10} compound family known as monoterpenes has especially received much attention in SOA studies, as some of the C_{10} compounds' oxidation products likely have sufficiently low volatilities to participate in new-particle formation.

Once peroxy radicals have been formed, a plethora of further reactions may occur. An important pathway with respect to aerosol formation is autoxidation, in which the peroxy radical moiety undergoes an intramolecular hydrogen-shift to form a hydroperoxide alkyl radical, which may again react with molecular oxygen to form a more oxygenated and complex peroxy radical compound.¹² This kind of reaction pathway can rapidly increase the oxygen content and the mass

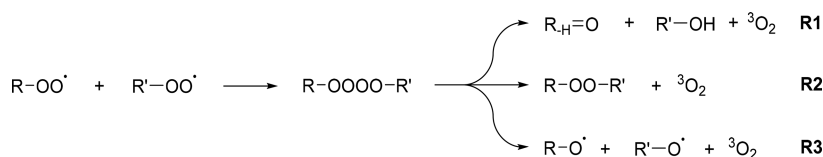
Received: February 24, 2022

Revised: May 25, 2022

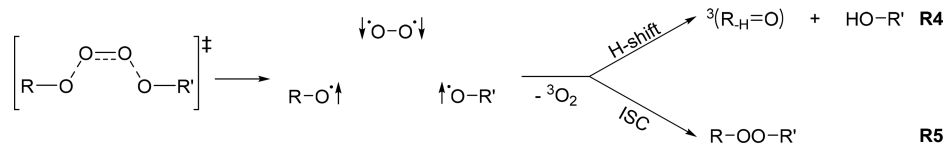
Published: June 16, 2022



Scheme 1. Intermolecular Self- and Cross-Reactions of Peroxyl Radicals



Scheme 2. Sequential Decomposition of a Tetroxide Intermediate into Triplet Molecular Oxygen and Alkoxy Radicals, and the Two Product Channels: H-Shift and ISC



of the molecule, giving rise to so-called highly oxygenated molecules (HOM).¹³ The radical propagation mechanism can terminate, for example, when the radical hydrogen abstraction occurs at a carbon containing a hydroperoxide group, as the $\bullet\text{C}-\text{OOH}$ group rapidly rearranges into a closed-shell carbonyl compound and a free hydroxyl radical.¹⁴

In addition to intramolecular reactions, peroxy radicals also react via intermolecular pathways. In high NO_x concentrations, peroxy radicals can react with $\text{NO}\bullet$ to produce alkoxy radicals and $\text{NO}_2\bullet$, or with $\text{NO}_2\bullet$ to produce peroxy nitrates. In low NO_x , peroxy radical radicals react mainly with $\text{HO}_2\bullet$ to form alkyl hydroperoxides.¹⁵

Although they are not the main channel for peroxy radical reactions, self- and cross-reactions with other peroxy radicals may play a central role in SOA formation.^{16,17} These reactions can be categorized into propagating reactions and terminating reactions. In the former, the radical character of the molecule(s) is retained and propagates to the next stage, while in the latter only closed-shell molecules are eventually produced, and the reaction chain thereby terminates. These two types of mechanisms are visualized in Scheme 1.

The current consensus is that the majority of peroxy radical cross-reactions occur through tetroxide intermediates as seen in Scheme 1.^{18–22} Few studies have elucidated the mechanisms involved in the formation of the tetroxide intermediate ($\text{RO}_4\text{R}'$) and in the subsequent decomposition into various product channels. The original study of tetroxide intermediates by Russell suggested a cyclic, concerted decomposition transition state into aldehyde/ketone, alcohol, and molecular oxygen (Scheme 1, R1).¹⁸ The end products of this mechanism have been experimentally verified to be the main products of primary and secondary peroxy radical self- and cross-reactions in the liquid phase (R1 is not possible for tertiary alkoxy radicals due to absence of α -oxy hydrogens). In the gas phase, both the alcohol + carbonyl (Scheme 1, R1) and alkoxy radicals (Scheme 1, R3) have substantial yields.^{23–25} However, the Russell mechanism itself has been deemed unlikely, as it is inconsistent with thermodynamic experiments and computational studies.^{26–29}

Seminal theoretical work by Ghigo et al.³⁰ investigated the decomposition reaction of dimethyltetroxide (MeO_4Me) with the CASSCF (Complete Active Space Self-Consistent Field) method.³¹ The initial effort in that study was to elucidate the cyclic decomposition of the tetroxide into alcohol and carbonyl products (Scheme 1, R1), but transition states corresponding to such a mechanism were not found. The possibility to decompose into singlet molecular oxygen and two alkoxy

radicals coupled into a singlet was deemed unlikely on thermodynamical grounds and not investigated further. Such a mechanism could still explain the experimental observation of singlet molecular oxygen. This led to the suggestion that the tetroxide may decompose first into triplet molecular oxygen and two doublet alkoxy radicals, adding up to a total singlet multiplicity (Scheme 1, R3, and Scheme 2). Then, after the initial decomposition, both the Russell-product channel (Scheme 2, R4) and dimerization channel (Scheme 2, R5) are available via intermolecular H-shift and intersystem crossing (ISC), respectively. Alkoxy radical formation (Scheme 1, R3) simply corresponds to dissociation of the product complex.

The original study by Ghigo et al.³⁰ suggested that ISC is important but did not provide any theoretical results on the matter. This motivated our previous work on thorough investigation of the intersystem crossings for the MeO_4Me model system.³² In later work, we used this approach for H-shifts and dimerization reactions for ${}^3(\text{RO}\cdots\text{R}'\text{O})$ complexes corresponding to several atmospherically relevant and model $\text{RO}_2\bullet + \text{R}'\text{O}_2\bullet$ systems.³³

In this work, we aim to complement our previous discoveries by completing the reaction path from the beginning. We elucidate the reaction pathway from the separate peroxy radicals to the tetroxide intermediate and finally to the decomposition of the tetroxide via the mechanism illustrated in the left-hand-side reaction of Scheme 2; the reaction pathway downstream of this decomposition is already covered by our previous work.³³

2. THEORETICAL METHODS

2.1. Conformational Sampling of Tetroxides, Peroxy Radicals, and Alkoxy Radicals. The investigated tetroxides, and most peroxy radicals and alkoxy radicals, have many conformational isomers. Systematic sampling of the conformational space was therefore carried out with the Spartan 16 program.³⁴ In the sampling, the torsional degrees of freedom (excluding the rotation of methyl groups) were scanned as a function of the potential energy calculated with the Merck Molecular Force Field (MMFF94) level of theory.³⁵ To avoid erroneous description of peroxy radicals and alkoxy radicals as anions instead of neutral radicals, the keyword `ffhint="Ox~6"` (x is the number of the terminal oxygen) was used to force the terminal oxygen to be a neutral radical. Unique local potential energy minimum conformers resulting from the sampling were then collected. More accurate

single-point energies for the conformers were obtained at the B3LYP/6-31+G(d)^{36–42} level of theory with Gaussian 16.⁴³ At this stage, a 5 kcal/mol threshold compared to the lowest-energy conformer was used as a cutoff for pruning the list of conformers. Molecular geometries of the remaining conformers were optimized at the B3LYP/6-311+G(d)^{37,44} level of theory. Duplicates based on close or identical total energies and dipole moment values were removed from the conformer list, and a cutoff of 2 kcal/mol was used to further limit the number of conformers. Finally, the remaining conformers were reoptimized at the ω B97X-D/aug-cc-pVTZ^{45–47} level of theory with Gaussian 16. The obtained global minimum conformers were used in further calculations.

The choice of the functionals and the corresponding basis sets in the conformational sampling follow the trend of increasing accuracy (and cost) as the number of conformers decreases throughout the sampling. This sampling methodology is based on the cost-effective scheme for unimolecular peroxy radical reactions developed by Møller et al.⁴⁸ and has been successfully employed in our past research on bimolecular peroxy radical reactions.^{32,33}

2.2. Geometry Optimization of the Stationary Points along the Reaction Coordinate with CASSCF/6-311++G(d,p). The active spaces in the CASSCF optimizations are constructed similarly to our previous studies, where we used the (10,8) active space for investigating the methyl peroxy self-reaction.³² A detailed description of how the active space was set up can be found in the [Supporting Information](#) (SI, Section S2). All CASSCF calculations were done with the Firefly QC package,⁴⁹ which is partially based on the GAMESS-US source code.⁵⁰ We used the state-specific formalism of the theory on a singlet potential energy surface.

In the geometry optimization, very tight numerical thresholds were used in all parts of the calculations. This choice was made because in Firefly, only numerical Hessian evaluations are available for MCSCF. The maximum allowed asymmetry in the Lagrangian matrix was set to 1.0×10^{-8} a.u. instead of the default 1.0×10^{-5} a.u. The SCF energy convergence criteria were changed from the default 1.0×10^{-10} a.u. to 1.0×10^{-12} a.u. Convergence criteria for the molecular geometry, defined in terms of the largest component of the gradient, were also tightened from the default value 1.0×10^{-4} a.u. to 7.0×10^{-6} a.u. All convergence criteria were relaxed to the default values for the 15 Å separated pair of RO₂• radicals and for the 2RO• + ³O₂ product complex. The presence of a frozen coordinate in the former system means that optimized structures would in any case not correspond to minima on the potential energy surface, so vibrational analyses were skipped altogether in this case. Convergence criteria were relaxed for the latter system due to difficulties in reaching geometry convergence (presumably at least partially due to a flat potential energy surface caused by the very limited interaction of O₂ with the alkoxy radicals).

To obtain consistent and comparable vibrational frequencies for the non-interacting RO₂• + RO₂• peroxy radical pair, the (10,8) active space was split in half into (5,4) active spaces for each RO₂•. The active space orbitals were chosen carefully to match the active space orbitals localized onto each of the RO₂• fragments in the (10,8) RO₂• + RO₂• pair. Furthermore, to confirm that the $2 \times (5,4)$ active space was size-consistent with the (10,8) active space, CASSCF(5,4)/6-311++G(d,p) single-point energies for all the RO₂• monomer geometries in the RO₂• + RO₂• pairs were calculated and compared against

CASSCF(10,8) energies. Afterward, geometry optimization and vibrational frequencies for the RO₂• structures were calculated with CASSCF(5,4)/6-311++G(d,p) using the same tightened criteria as described previously. The results of the size-consistency analysis, which indicates that the CASSCF “split active space” results are size-consistent while the corresponding XMC-QDPT2 (Extended Multi-Configurational Quasi-Degenerate Perturbation Theory at Second Order of Perturbation) results are not, can be found from the SI).

For transition state calculations, fully numerical Hessians were calculated at the beginning of all first-order saddle-point optimizations. For both minima and transition states, the full numerical Hessian was calculated at the end of the geometry optimization to verify the nature of the obtained stationary points. Minima were identified by positive-definite Hessian matrices. In a few cases, due to the numerical nature of Hessian analysis, some imaginary frequencies persisted, but they were verified to correspond to either translational or rotational modes via Sayvetz condition analysis.⁵¹ The corresponding structures were exclusively either loosely bound reactant complexes or 15 Å separated peroxy radicals. Transition state structures were also identified by their Hessian matrices, having only one negative eigenvalue (all others non-negative) with a related eigenvector corresponding to motion along the reaction coordinate. The corresponding imaginary vibrational frequencies can be found for all transition states in the SI section listing the optimized geometries from CASSCF(10,8) and CASSCF(5,4) calculations (SI, Section S10). The numerical Hessians were calculated with doubled displacements (0.005 a.u. displacement in both positive and negative direction, 7-point stencil) in all three Cartesian directions to reach better accuracy.

2.3. XMC-QDPT2(10,8) Single-Point Calculations. XMC-QDPT2(10,8)/6-311++G(d,p) optimizations for the CH₃O₂• + CH₃O₂• system were carried out in our previous study.³² Due to the computationally demanding nature of XMC-QDPT2(10,8)/6-311++G(d,p) calculations,⁵² further geometry optimizations were not conducted at this level of theory in this study. Instead, single-point total energy calculations were carried out on the CASSCF(10,8) optimized geometries of all stationary points to better take into account dynamic electron correlation effects within the investigated systems. SCF convergence criteria were relaxed in a similar manner to the CASSCF calculations, for the 15 Å separated RO₂• pairs and 2 RO• + ³O₂ structures. XMC-QDPT2 calculations were done with the Firefly QC package.⁴⁹

2.4. ASCI-SCF/PT2 Single-Point Calculations. The adaptive sampling configuration interaction (ASCI) method⁵³ enables accurate multiconfigurational calculations in large active spaces. We employed the ASCI-SCF (ASCI self-consistent field) method⁵⁴ to further validate the CASSCF(10,8) method. Full-valence ASCI-SCF calculations were carried out for the HO₄H, MeO₄H, and MeO₄Me systems at the corresponding CASSCF geometries in the 6-311++G(d,p), cc-pVDZ, and the cc-pVTZ basis sets.⁴⁷ ASCI-SCF orbital optimization was carried out with ASCI wave functions containing 10⁵ determinants. These orbitals were then employed in further ASCI calculations. The ASCI and ASCI-SCF calculations were carried out with a development version of Q-Chem versions 5.4 and 5.4.1.⁵⁵

The effect of the truncation of the ASCI wave function was studied in two ways: by increasing the number of variationally determined determinants from 10⁵ to 5×10^6 and/or by

examining perturbative corrections to the ASCI energy. The results appear to be converged beyond the required accuracy, especially when the perturbative correction is used. The ASCI results, which support our central findings, are discussed in the SI (Section S7).

2.5. Coupled-Cluster Single-Point Calculations for Tetroxides, Peroxyl Radicals, and Alkoxy Radicals.

Coupled-cluster single-point total energies were calculated for structures that were reasonably well described with single reference wave functions. These structures were the free peroxy radicals, the intermediate tetroxides, the free alkoxy radicals, and triplet molecular oxygen. The density functional theory (DFT)-optimized global minimum conformer geometries were used for all coupled-cluster calculations. The level-of-theory for coupled-cluster calculations was CCSD(T)-F12a/cc-pVDZ-F12,^{56,57} as implemented in Molpro.⁵⁸ Some structures were too large to be calculated with canonical coupled-cluster, so those were calculated with DLPNO-CCSD(T)-F12/cc-pVTZ-F12,⁵⁹ as implemented in ORCA-4.2.1.^{60,61} The DLPNO-CCSD(T)-F12 parameters were tuned to match the canonical CCSD(T)-F12a energies as closely as possible. This was done by calculating both the CCSD(T)-F12a/cc-pVDZ-F12 and DLPNO-CCSD(T)-F12 energies for the largest system, where CCSD(T)-F12a was still applicable. The only change that had any appreciable effect was the increase of the basis set size from the cc-pVDZ-F12 to cc-pVTZ-F12 for the DLPNO calculations.

A great deal of care was taken when choosing the Hartree-Fock (HF) reference wave function for coupled-cluster calculations. It is a well-known problem that HF calculations may converge to only local minima or even saddle-point solutions instead of the global minimum.^{62,63} To find the global minimum HF wave function, the original SCF solution was perturbed with a series of orbital mixings, and the perturbed wave function was then reoptimized.⁶² The lowest energy HF wave function was then used for the coupled-cluster calculations. Further details on this method can be found in the SI (Section S1).

2.6. Thermochemistry. The thermochemical parameters were computed for all tetroxides, peroxy radicals, alkoxy radicals, as well as triplet and singlet molecular oxygen, at the ω B97X-D/aug-cc-pVTZ level of theory. Vibrational analyses were carried out for the DFT-optimized global minimum structures, and the subsequent thermochemical data was calculated at 298.15 K and 1 atm pressure. Total Gibbs energies were calculated by adding the Gibbs energy correction from the thermochemistry calculation to the total energy calculated with CCSD(T)-F12a/cc-pVDZ-F12 or DLPNO-CCSD(T)-F12/cc-pVTZ-F12 level of theory. For the smallest systems, namely, HO•, HO₂•, MeO•, MeO₂•, and ³O₂, improved total energies were also calculated with the W2-F12 thermochemical recipe.⁶⁴ The vibrational frequencies used in the Gibbs energy correction term were scaled by a factor of 0.957, as is suggested for the ω B97X-D/aug-cc-pVTZ in the CCCDBD (Computational Chemistry Comparison and Benchmark Database) vibrational scaling factor database.⁶⁵

In addition to DFT thermochemistry, vibrational analyses were carried out with CASSCF(5,4)/6-311++G(d,p) for RO₂• and with CASSCF(10,8)/6-311++G(d,p) for the RO₂•••R'O₂ cluster, the tetroxide formation transition state (ROO•••OOR')[‡], the tetroxide minimum RO₄R', and the decomposition transition state (RO•••O₂•••OR')[‡]. All CASSCF thermochemical calculations were conducted using the

corresponding CASSCF-optimized geometries at 298.15 K and 1 atm pressure. The vibrational frequencies used in the Gibbs energy correction term were scaled with a factor of 0.906, which is the suggested value for HF/6-311+G(3df,2pd), the closest level of theory to CASSCF/6-311++G(d,p) available in the CCCDBD database.⁶⁵

3. RESULTS AND DISCUSSION

3.1. Model Systems. The model systems for this study were chosen by considering various atmospheric reaction pathways that produce primary and secondary peroxy radicals. Tertiary peroxy radicals are believed to have slow self- and cross-reaction rates¹⁷ and are therefore not studied in this work. The question on the universality of the commonly assumed trend of slow rates for tertiary systems will be investigated in a follow-up study.

Simple alkylperoxy radicals such as methyl-, ethyl-, and *i*-propylperoxy radicals (MeO₂•, EtO₂•, *i*PrO₂•) are derived from alkanes by hydrogen abstraction by HO• or NO₃•, followed by the addition of O₂. Acyl- and acetyl peroxy radicals (AcO₂•, AceO₂•) are similarly formed by hydrogen abstraction followed by O₂ addition from acetaldehyde and acetone, respectively. The two hydroxylated peroxy radicals, *R*- and *S*-1-hydroxy-butan-2-ylperoxy radicals (hereinafter denoted as *R*-BuOH-O₂• and *S*-BuOH-O₂•), are produced by HO• addition to the terminal unsaturated carbon of a 1-butene molecule, and subsequent addition of molecular oxygen to the second carbon, leading to formation of an enantiomeric mixture of *R* and *S* isomers. The two peroxy radicals containing a nitrate group are similarly formed by addition of a nitrate radical to the terminal unsaturated carbon of 1-propene and subsequent addition of molecular oxygen, also producing an enantiomeric mixture of *R*- and *S*-2-peroxypropyl nitrate (hereinafter denoted as *R*-PrNO₃-O₂• and *S*-PrNO₃-O₂•). The hydroperoxy radical (HO₂•) is known to react predominantly via mechanisms other than the tetroxide pathway in the atmospheric conditions, but it was studied as the smallest possible model compound for tetroxide formation. The last of the studied systems, the allylperoxy radical (AllylO₂•), is not necessarily an atmospherically relevant model compound, but it is studied to see whether unsaturation near the peroxy moiety makes a difference in the reactivity. Most of the studied tetroxides and the decomposition products thereof are formed from two identical peroxy radicals, but three unsymmetric tetroxides, MeO₄H, AcO₄Me, and AceO₄-*S*-BuOH, are also investigated. In addition, both *R,R*- and *R,S*-tetroxide products of *R*-BuOH-O₂•, *S*-BuOH-O₂•, *R*-PrNO₃-O₂•, and *S*-PrNO₃• are considered.

3.2. Thermodynamics of Tetroxide Formation and Decomposition. The thermodynamics of the overall reaction was investigated by calculating ω B97X-D/aug-cc-pVTZ global minimum geometries and the corresponding vibrational frequencies for all RO•, RO₂•, RO₄R', ³O₂, and ¹O₂ structures (Table 1). Total energies for more accurate Gibbs energies were calculated with either CCSD(T)-F12a/cc-pVDZ-F12 or DLPNO-CCSD(T)-F12/cc-pVTZ-F12. Two decomposition channels were considered, one in which molecular oxygen is formed in the ground triplet state and another in which molecular oxygen is formed in an excited singlet state.

The relative energy differences in the thermodynamic profile of the overall reaction (Table 1) were obtained by comparing the Gibbs energies of two separate peroxy radicals to the energy of the tetroxide and to the total energy of two alkoxy

Table 1. Gibbs Energy Changes in the Tetroxide Formation and Decomposition^a

R ^b	R' ^b	Gibbs energy change (ΔG), kcal/mol		
		RO ₂ • + R'O ₂ •	RO ₄ R'	RO• + R'O• + ³ O ₂
H	H	0.00	-5.15	3.43
Me	H	0.00	-2.52	-2.05
Me	Me	0.00	-1.48	-7.53
Et	Et	0.00	-1.31	-4.72
iPr	iPr	0.00	-1.08	-3.91
Ac	Me	0.00	-8.36	-12.70
Ac	Ac	0.00	-12.22	-17.88
Allyl	Allyl	0.00	-1.27	-8.15
Ace	Ace	0.00	-2.90	-9.67
Ace	Ace	0.00 ^c	1.29 ^c	-10.43 ^c
Ace	S-BuOH	0.00 ^c	-0.48 ^c	-9.48 ^c
R-BuOH	R-BuOH	0.00 ^c	0.79 ^c	-8.52 ^c
R-BuOH	S-BuOH	0.00 ^c	-0.09 ^c	-8.52 ^c
R-PrNO ₃	R-PrNO ₃	0.00 ^c	0.25 ^c	-8.17 ^c
R-PrNO ₃	S-PrNO ₃	0.00 ^c	0.01 ^c	-8.24 ^c

^aGibbs energies were calculated by adding Gibbs energy corrections (ω B97X-D/aug-cc-pVTZ, 298 K, 1 atm reference pressure) to the CCSD(T)-F12a/cc-pVDZ-F12 total energies. ^bData for R or R' = H is presented for reference and comparison only: the dominant reaction pathway in these systems is not the mechanism studied here. ^cTotal energies have been calculated with DLPNO-CCSD(T)-F12/cc-pVTZ-F12 instead of CCSD(T)-F12a/cc-pVDZ-F12 for computational reasons.

radicals and molecular oxygen. Thus, the energies listed in Table 1 describe the thermodynamic picture in the limit of no interaction between the various fragments. However, if molecular oxygen were to form in a singlet state, then the two alkoxy radicals would form as doublets coupled into a singlet, thus allowing the possible direct formation of ROOR' products, substantially lowering the total energy part of the Gibbs energy. This reaction route is still highly unlikely for all the studied systems because the decomposition into singlet molecular oxygen is very endergonic (¹O₂ is above the ³O₂ in Gibbs energy by 29.61 kcal/mol at CCSD(T)-F12a/cc-pVDZ-F12 and by 32.10 kcal/mol at DLPNO-CCSD(T)-F12/cc-pVTZ-F12). In comparison, every reaction producing triplet molecular oxygen (except HO₂• + HO₂• → HO• + HO• + ³O₂) is exergonic and therefore very likely to be the main reaction pathway.

The formation of the tetroxide intermediate is also thermodynamically feasible. For all systems where the total energy is calculated with the CCSD(T)-F12a method, the relative Gibbs energy change is negative for the tetroxide formation. For one tetroxide structure (AceO₄Ace), both CCSD(T)-F12a and DLPNO-CCSD(T)-F12 total energies were calculated, and the canonical CCSD(T)-F12a suggests exergonic formation while DLPNO-CCSD(T)-F12 indicates slightly endergonic formation. As canonical CCSD(T)-F12a results are more accurate than DLPNO-CCSD(T)-F12 (DLPNO converges to canonical results if threshold values are infinitely tightened), this suggests that formation of tetroxide intermediates are an exergonic process for all the studied systems.

More accurate Gibbs energy changes were calculated for the three smallest systems with a modified explicitly correlated W2-F12 thermochemical protocol. The tetroxide intermediates were not calculated with this method. Results from these

calculations are illustrated in Table 2 along with Gibbs energy changes calculated at the ω B97X-D/aug-cc-pVTZ and CCSD-

Table 2. Gibbs Energy Change of the Overall Reaction, Comparison of Methods

reaction ^a	Gibbs energy change (ΔG), kcal/mol		
	ω B97X-D/ aug-cc-pVTZ	CCSD(T)-F12a/ cc-pVDZ-F12 ^b	W2-F12 ^c
HO ₂ • + HO ₂ • → HO• + HO• + ³ O ₂	5.94	3.43	4.88
MeO ₂ • + HO ₂ • → MeO• + HO• + ³ O ₂	-2.17	-2.05	-0.84
MeO ₂ • + MeO ₂ • → MeO• + MeO• + ³ O ₂	-10.28	-7.53	-6.56

^aData for reactions with HO₂• is presented for reference and comparison only: the dominant reaction pathway in these systems is not the mechanism studied here. ^bThermal corrections to CCSD(T)-F12a/cc-pVDZ-F12 total energies were calculated at ω B97X-D/aug-cc-pVTZ. ^cGeometries and frequencies were calculated with ω B97X-D/aug-cc-pVTZ instead of B3LYP/cc-pV(T+d)Z. Gibbs energy correction was scaled with a factor of 0.957.

(T)-F12a/cc-pVDZ-F12 levels of theory. Increasing the accuracy appears to decrease the change in the Gibbs energy (i.e., the reaction free energies become less negative), except for the 2 HO₂• → 2 HO• + O₂ reaction, where such a trend is not observed (Table 2).

Another motivation for producing CCSD(T)-F12a/cc-pVDZ-F12 total energies at ω B97X-D/aug-cc-pVTZ optimized geometries for peroxy radicals and alkoxy radicals is the apparent discrepancy between CASSCF and XMC-QDPT2 results (Sections 3.3 and 3.4) for separated peroxy radicals and for the dissociation products of tetroxides. CASSCF predicts much smaller electronic energy differences between separated peroxy radicals and tetroxides than coupled cluster does. Because peroxy radicals and alkoxy radicals are well described in the single reference DFT-formalism, the coupled-cluster corrected DFT results are probably more accurate than those from CASSCF or even from XMC-QDPT2 for the thermodynamics of the overall reaction. These energies are shown for all the studied systems in the SI (Section S9).

3.3. CASSCF(10,8)/6-311++G(d,p) Optimized Reaction Pathway. The whole reaction pathway starting from two separated peroxy radicals (separated by 15 Å) all the way to the decomposition into two alkoxy radicals and triplet molecular oxygen was studied at the CASSCF(10,8)/6-311++G(d,p) level of theory. The computational details, including the setup of the active space, are discussed in the SI (Section S2), and the results from the reaction pathway optimizations are shown in Table 3.

All the systems studied have local minima corresponding to a loosely bound peroxy radical pair (reactant complex; RO₂...R'O₂) which is lower in electronic energy than the separated pair of peroxy radicals (RO₂• + R'O₂•). At the CASSCF level, this loosely bound cluster is lower in energy than the tetroxide intermediate in all systems, except for the AcO₂...AcO₂ and AcO₂...MeO₂ clusters, where the tetroxides are lower in energy by 8.66 and 4.66 kcal/mol, respectively. These two systems are also unique in that the formation reaction of the tetroxide from the peroxy pair cluster appears to be barrierless. A relaxed surface scan starting from the tetroxide intermediate and lengthening the inner O-O bond showed that the electronic energy increases as a function of the separation of the oxygen

Table 3. CASSCF(10,8) Optimized Stationary Points and XMC-QDPT2(10,8) Single-Point Energies along the Reaction Coordinate^a

R ^b	R' ^b	relative energy difference, kcal/mol						
		RO ₂ • + R'O ₂ • ^c	RO ₂ ...R'O ₂	[ROO...OOR'] [‡]	RO ₄ R'	[RO...O ₂ ...OR'] [‡]	RO• + R'O• + ³ O ₂	
H	H	3.92 8.42 (19.17)	-0.32 2.95	4.19 4.13	0.00	2.34 1.71	-12.46 9.57 (33.10)	
Me	H	3.09 10.88 (16.72)	-1.23 4.06	3.87 4.65	0.00	1.21 1.03	-16.63 12.62 (27.22)	
Me	Me	0.88 3.72 (16.19)	-1.27 -0.56	1.40 -3.00	0.00	2.31 -3.42	-17.41 3.98 (23.26)	
Et	Et	0.69 10.71 (15.14)	-1.73 5.38	1.53 -0.30	0.00	1.21 -0.74	-18.37 13.64 (24.41)	
iPr	iPr	-0.47 6.98 (15.24)	-2.92 1.23	1.06 -3.69	0.00	2.97 -5.40	-17.17 12.08 (25.06)	
Ac	Me	7.48 19.37 (22.33)	4.66 15.82	^d	0.00	1.09 -0.44	-20.33 14.30 (23.49)	
Ac	Ac	12.23 32.04 (27.43)	8.66 26.33	^d	0.00	0.05 -0.99	-23.94 16.59 (22.68)	
Allyl	Allyl	1.31 14.30 (16.52)	-1.06 10.41	2.73 3.67	0.00	0.71 0.32	-20.17 18.02 (23.51)	
Ace	Ace	2.36 19.65 (17.94)	-0.73 14.24	3.41 5.10	0.00	0.91 0.72	-22.92 18.66 (22.75)	
Ace	S-BuOH	3.67 21.28 (16.67) ^e	-1.64 13.48	3.26 3.58	0.00	1.35 -2.82	-21.49 45.69 (22.30) ^e	
R-BuOH	R-BuOH	3.02 21.55 (14.56) ^e	-2.40 13.45	6.64 6.76	0.00	1.11 -3.25	-21.86 47.58 (21.80) ^e	
R-BuOH	S-BuOH	3.57 20.00 (15.24) ^e	-1.57 14.26	3.52 2.52	0.00	1.36 -3.65	-20.87 18.70 (22.49) ^e	
R-PrNO ₃	R-PrNO ₃	3.44 28.03 (15.27) ^e	-1.82 18.61	3.72 5.08	0.00	1.46 -5.11	-22.52 50.56 (22.02) ^e	
R-PrNO ₃	S-PrNO ₃	4.02 28.40 (14.94) ^e	-1.32 17.50	2.73 2.14	0.00	2.18 -4.59	-21.65 25.09 (21.78) ^e	

^aLightfaced values correspond to CASSCF energies, and bold values correspond to XMC-QDPT2 single-point energies. For comparison, values in brackets correspond to CCSD(T)-F12a/cc-pVDZ-F12 single-point total energies at ω B97X-D/aug-cc-pVTZ optimized geometries. ^bData for R or R' = H is presented for reference and comparison only: the dominant reaction pathway in these systems is not the mechanism studied here. ^cIn the geometry optimizations, the distance between the two terminal oxygen atoms of the peroxy moieties were frozen to 15 Å. ^dBarrierless formation reaction. ^eDLPNO-CCSD(T)-F12/cc-pVTZ-F12 used instead of CCSD(T)-F12a/cc-pVDZ-F12.

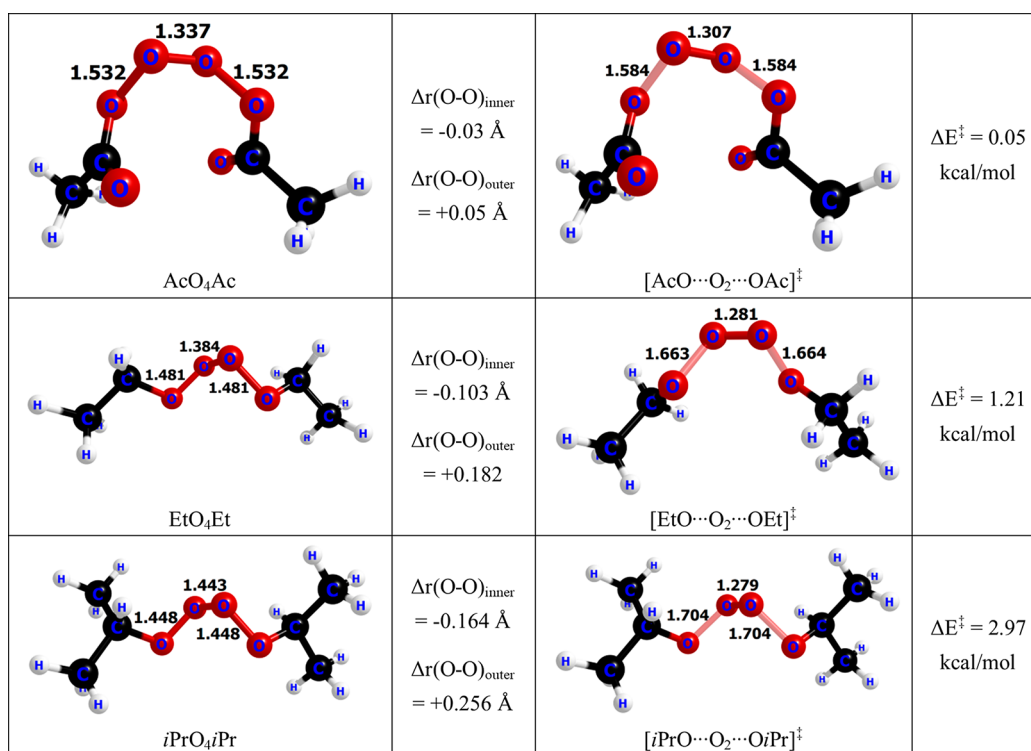


Figure 1. Changes in the different O–O bond lengths in the tetroxide decomposition and their relation to the CASSCF barrier height.

atoms. This behavior was found originally only for AcO₂• + AcO₂•; the nonidentical pair of AcO₂• + MeO₂• was studied afterward to see whether only one acylperoxy radical is enough to make the formation reaction barrierless. The prereactive complex of these two systems corresponds to an inflection point on the potential energy surface rather than a true minimum point in a potential well. AcO₂• + AcO₂• and AcO₂• + MeO₂• also have the highest excess energy in comparison to the tetroxide intermediate (i.e., the tetroxide is the most strongly bound compared to the free reactants). For

all the other studied systems, a transition state for the formation of the tetroxide was found, with barrier heights (total energies, compared to the reactant complex) ranging from 2.67 to 9.04 kcal/mol. The highest barrier corresponds to the formation of the R-BuOH-O₄-R-BuOH—all other barrier heights range from 2.67 to 5.54 kcal/mol.

The barrier heights for the decomposition reaction are smaller than those for the formation reaction. The decomposition barriers range from 0.05 to 2.97 kcal/mol. The lowest decomposition barrier is found for [AcO...O₂...OAc][‡], while

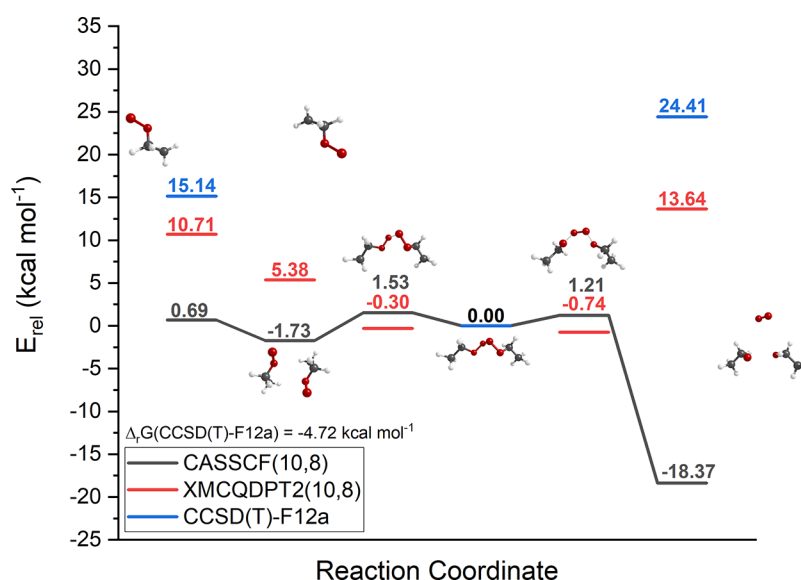


Figure 2. CASSCF optimized reaction pathway (gray) with XMC-QDPT2 single-point energies (red) and CCSD(T)-F12a single-point energies (blue) (CCSD(T)-F12a energies are calculated on DFT-optimized geometries). Reaction of EtO_4Et shown as an example.

the highest barrier is found for $[\text{iPrO}\cdots\text{O}_2\cdots\text{OiPr}]^\ddagger$. Differences between the barrier heights can be attributed to changes in O–O bond lengths that the tetroxide undergoes to decompose. For example, the O–O bond lengths in the AcO_4Ac change very little when going from the tetroxide intermediate to the decomposition transition state geometry $[\text{AcO}\cdots\text{O}_2\cdots\text{OAc}]^\ddagger$, whereas the changes are more pronounced between the iPrO_4iPr tetroxide and the $[\text{iPrO}\cdots\text{O}_2\cdots\text{OiPr}]^\ddagger$ transition state geometry. This trend is displayed in Figure 1.

The steep decrease in relative total energies from the tetroxides to the $\text{RO}\bullet + \text{R}'\text{O}\bullet + {}^3\text{O}_2$ products at the CASSCF level is not replicated in XMC-QDPT2 and coupled-cluster calculations (see Table 3 and Figure 2). Both XMC-QDPT2 and coupled-cluster results suggest a rise in total energy in comparison to the decomposition transition state. The decomposition of a tetroxide into two radicals and molecular oxygen is most likely an endothermic process, so the coupled-cluster and XMC-QDPT2 total energies for the products are arguably also more chemically reasonable. However, the entropic boost of forming three product molecules from two reactants still drives the overall reaction to be exergonic, as demonstrated in the previous section (Table 1). Additionally, it has been demonstrated in our previous studies that the subsequent reactions of the alkoxy radicals, including both H-shifts, dissociation, and recombination following intersystem crossings (Scheme 1, R1–R3) all have extremely high reaction rates.

3.4. XMC-QDPT2(10,8)/6-311++G(d,p) Single-Point Energies. CASSCF energies were corrected with XMC-QDPT2 single-point energy calculations using the CASSCF-optimized molecular geometries. The motivation for calculating XMC-QDPT2 energies was to alleviate the lack of dynamical correlation in CASSCF. As discussed above, although the XMC-QDPT2 corrections do not appear to be fully compatible with CASSCF geometries, they provide useful further insights into the reactions. The XMC-QDPT2 single-point energies predict the transition states, for both the formation and the decomposition of the tetroxide, to be lower in energy than the tetroxide itself, in multiple studied systems (see boldfaced values in Table 3, and Figure 2). This result is

in apparent contradiction with our previous work, in which we found qualitatively similar reaction pathways for MeO_4Me formation and decomposition at the XMC-QDPT2(10,8)/6-311++G(d,p) and CASSCF(10,8)/6-311++G(d,p) levels of theory. The crucial difference is that in our previous work, the molecular geometries of the MeO_4Me were also optimized at the XMC-QDPT2(10,8)/6-311++G(d,p) level of theory. When this is done, the barrier heights are comparable between the methods, with formation barriers of 2.67 and 1.43 kcal/mol and decomposition barriers of 2.31 and 0.74 kcal/mol using CASSCF and XMC-QDPT2, respectively (Figure 3). Unfortunately, the extremely high cost of XMC-QDPT2 geometry optimizations prevents us from carrying them out for the larger systems studied here.

Even though the XMC-QDPT2 single-point transition states are lower in total energy than the tetroxide intermediates, the formation transition state is consistently higher in energy than the decomposition transition state, across all studied systems. This agrees qualitatively with both the CASSCF optimized reaction pathways and the XMC-QDPT2 optimized reaction pathway for the MeO_4Me reaction. All obtained results thus indicate that the formation of the tetroxide is the rate-limiting step in the total reaction pathway, and the barrier for this formation step is unlikely to be insurmountably high at least for primary and secondary peroxy radicals. The latter finding is further verified by ASCI-SCF single-point energy calculations (SI Section S7) on the MeO_4Me system.

The XMC-QDPT2 optimizations reported in our previous study suggest that the loosely bound $\text{MeO}_2\cdots\text{MeO}_2$ reactant complex is higher in energy than the tetroxide, while the CASSCF results of this work indicate that the reactant complexes are generally lower in energy than the tetroxide (Figures 2 and 3).

The absolute differences in relative energies with respect to the tetroxide intermediate (Table 3) between CASSCF and XMC-QDPT2 are largest for the stationary points where interactions are noticeably different from those in the tetroxide, due to either the presence of long-range interactions ($\text{RO}_2\cdots\text{R}'\text{O}_2$ and $\text{RO}\cdots\text{O}_2\cdots\text{R}'\text{O}$) or the complete separation of the fragments ($\text{RO}_2\bullet + \text{R}'\text{O}_2\bullet$). For $\text{RO}_2\bullet + \text{R}'\text{O}_2\bullet$, $\text{RO}_2\cdots\text{R}'\text{O}_2$,

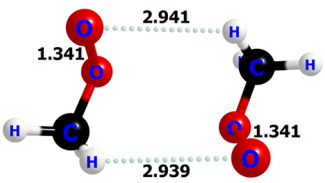
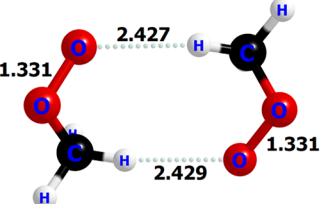
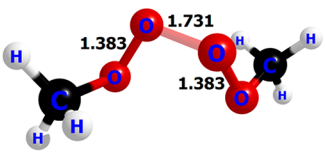
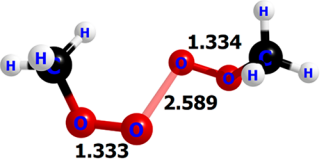
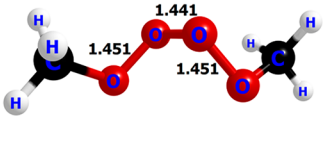
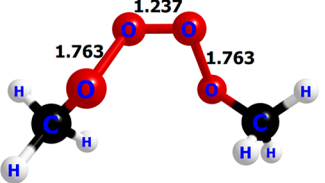
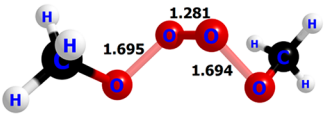
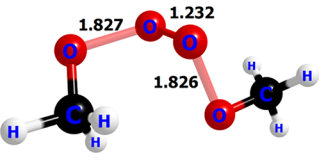
CASSCF(10,8)/6-311++G(d,p)	Δ (CASSCF vs. XMC- QDPT2)	XMC-QDPT2(10,8)/6-311++G(d,p)
 <p>MeO₂...MeO₂, E = -1.27 kcal/mol</p>	→	 <p>MeO₂...MeO₂, E = 6.12 kcal/mol</p>
↓ $\Delta r(\text{O-O})_{\text{out}} = +0.042 \text{ \AA}$ ↓	$\Delta r(\text{O-O})_{\text{out}} = -0.010 \text{ \AA}$	↓ $\Delta r(\text{O-O})_{\text{out}} = +0.002 \text{ \AA}$ ↓
 <p>[MeOO...OOMe][‡], E = 1.40 kcal/mol</p>	→	 <p>[MeOO...OOMe][‡], E = 7.55 kcal/mol</p>
↓ $\Delta r(\text{O-O})_{\text{out}} = +0.068 \text{ \AA}$ $\Delta r(\text{O-O})_{\text{in}} = -0.290 \text{ \AA}$ ↓	$\Delta r(\text{O-O})_{\text{out}} = -0.050 \text{ \AA}$ $\Delta r(\text{O-O})_{\text{in}} = +0.858 \text{ \AA}$	↓ $\Delta r(\text{O-O})_{\text{out}} = +0.430 \text{ \AA}$ $\Delta r(\text{O-O})_{\text{in}} = -1.352 \text{ \AA}$ ↓
 <p>MeO₄Me, E = 0.00 kcal/mol</p>	→	 <p>MeO₄Me, E = 0.00 kcal/mol</p>
↓ $\Delta r(\text{O-O})_{\text{out}} = +0.244 \text{ \AA}$ $\Delta r(\text{O-O})_{\text{in}} = -0.160 \text{ \AA}$ ↓	$\Delta r(\text{O-O})_{\text{out}} = +0.312 \text{ \AA}$ $\Delta r(\text{O-O})_{\text{in}} = -0.204 \text{ \AA}$	↓ $\Delta r(\text{O-O})_{\text{out}} = +0.064 \text{ \AA}$ $\Delta r(\text{O-O})_{\text{in}} = -0.005 \text{ \AA}$ ↓
 <p>[MeO...O₂...OMe][‡], E = 2.31 kcal/mol</p>	→	 <p>[MeO...O₂...OMe][‡], E = 0.74 kcal/mol</p>
↓ $\Delta r(\text{O-O})_{\text{out}} = +0.132 \text{ \AA}$ $\Delta r(\text{O-O})_{\text{in}} = -0.049 \text{ \AA}$ ↓	$\Delta r(\text{O-O})_{\text{out}} = +0.132 \text{ \AA}$ $\Delta r(\text{O-O})_{\text{in}} = -0.049 \text{ \AA}$	↓ $\Delta r(\text{O-O})_{\text{out}} = +0.132 \text{ \AA}$ $\Delta r(\text{O-O})_{\text{in}} = -0.049 \text{ \AA}$ ↓

Figure 3. Comparison of geometry optimizations using CASSCF and XMC-QDPT2. XMC-QDPT2 structures and energies are reproduced from our previous work.³²

and RO...O₂...R'O, the average of energy differences between the methods are 14.15, 11.56, and 41.78 kcal mol⁻¹, respectively. For the two transition states, [ROO...OOR'][‡] and [RO...O₂...OR'][‡], the relative difference between CASSCF and XMC-QDPT2 is much smaller, 1.48, and 2.73 kcal/mol, respectively.

The difference between CASSCF and XMC-QDPT2 for describing the loosely bound structures can be attributed to the lack of dispersion in CASSCF.⁶⁶ Differences in the transition state energies and tetroxide energies may be caused by the differences in optimal O–O bond lengths between the methods. The comparison of the CASSCF optimized molecular geometries from this study and the XMC-QDPT2 optimized molecular geometries from our previous study for MeO₄Me formation and decomposition³² reveal drastically different O–O bond lengths along the reaction pathway (Figure 3).

Additionally, the slight differences in optimal bond lengths and in the description of long-range interactions between the methods lead to different conformations in the optimized

structures. To provide more rigorous comparison of the methods, we tried to reoptimize CASSCF-geometries for MeO₄Me stationary points with XMC-QDPT2 and *vice versa*. Unfortunately, no convergence to directly comparable structures were obtained by either approach.

3.5. Bimolecular Reaction Rates. The overall bimolecular reaction rate coefficients were calculated using elementary transition state theory (TST) and CASSCF energetics. The computed reaction rate coefficients are predominantly smaller than the available experimental values (SI Table S4). The AcO₄Ac system is the exception to this trend, as the calculated rate slightly exceeds the experimental values. (The calculated rate also exceeds the gas-kinetic collision rate, implying that the conventional TST rate expression is not applicable for this case). For the other studied systems, the smaller rate coefficients may be due to the substantial underestimation of the excess total energies of the peroxy radicals (as compared to both the tetroxides and especially the formation transition states) at the CASSCF level of theory. As can be seen in Table 3, the coupled-cluster calculations suggest systematically higher

electronic energies for the peroxy radicals, which in turn would lower the ΔG^\ddagger correspondingly and enhance the reaction rate.

As discussed above, our results strongly indicate that the rate-limiting step for the studied $\text{RO}_2 + \text{R}'\text{O}_2$ reactions is the formation of either the $\text{RO}_4\text{R}'$ tetroxide or the $\text{RO}_2\cdots\text{R}'\text{O}_2$ complex. While the transition state corresponding to decomposition of the $\text{RO}_4\text{R}'$ cannot be modeled without multireference methods, the transition state for tetroxide formation can be qualitatively described also by DFT, for example. Thus, reasonable estimates of the overall reaction rates could plausibly be obtained by combining master equation modeling with coupled-cluster corrected DFT results on the $\text{RO}_4\text{R}'$ tetroxide and its formation TS, as well as by long-range transition state theory⁶⁷ for treating $\text{RO}_2\cdots\text{R}'\text{O}_2$ formation. We performed such modeling on systems for which experimental data is available and for which accurate canonical CCSD(T)-F12a energy calculations could be performed, using the MESMER program (see details in SI section S5).⁶⁸ The overall reaction rates obtained by this approach (SI Table S5) are generally even closer to the experimental values than those obtained using CASSCF energetics, and the ordering of the rates is fully correct: $k(\text{iPrO}_4\text{iPr}) < k(\text{EtO}_4\text{Et}) < k(\text{MeO}_4\text{Me}) < k(\text{AceO}_4\text{Ace}) < k(\text{AcO}_4\text{Me}) < k(\text{AcO}_4\text{Ac})$. The errors are largest for the fastest reactions, presumably due to the limitations in modeling barrierless formation of tetroxides from the $\text{RO}_2\cdots\text{R}'\text{O}_2$ complexes. We demonstrated in a very recent study^{69,70} that the experimental rates for $\text{RO}_2 + \text{R}'\text{O}_2$ reactions with submerged barriers can be predicted surprisingly well simply based on $\text{RO}_2\cdots\text{R}'\text{O}_2$ complex lifetimes estimated from nonreactive classical molecular dynamics simulations. These two sets of results now provide a complete toolbox for estimating at least order-of-magnitude accuracy rates for overall $\text{RO}_2\cdots\text{R}'\text{O}_2$ reactions in both the presence and the absence of substantial barriers for tetroxide formation. Unfortunately, predicting quantitative branching ratios for the various product channels will still require substantial further work.

4. CONCLUSIONS AND ATMOSPHERIC IMPLICATIONS

We have investigated the formation and decomposition pathways for tetroxide intermediates formed in the recombination of multiple atmospherically relevant primary and secondary peroxy radical model compounds at the CASSCF/6-311++G(d,p) level of theory. We showed that the barrier heights for both formation and decomposition are small in comparison to the excess energy of the peroxy radicals, suggesting that the studied reaction mechanism is a plausible pathway for the formation and decomposition of tetroxide intermediates in the atmosphere. XMC-QDPT2 single-point energy corrections agree with CASSCF in that the formation transition state is higher in energy than the decomposition transition state, which in turn suggests that the formation of the tetroxide (or in some cases that of the $\text{RO}_2\cdots\text{R}'\text{O}_2$ complex) is likely the rate-limiting step of the total reaction.

We observed several qualitative discrepancies between CASSCF results and XMC-QDPT2 single-point energies. A comparison of optimized reaction pathways for MeO_4Me suggests that the discrepancies are likely due to the lack of XMC-QDPT2 optimizations caused by computational limitations. In future research on similar systems, it would be

beneficial to employ methods with a better description of both static and dynamical correlation, and especially weak interactions such as H-bonds, in the geometry optimizations. At the time of this study, full geometry optimizations with, for example, XMC-QDPT2, ASCI-SCF(PT2), or multireference DFT methods are not yet widely applicable for large systems.

Thermodynamic calculations at the DFT+CCSD(T) level indicate that even though the product alkoxy radicals are likely to be higher in total energy than the tetroxide intermediates, the overall reaction is spontaneous with respect to the Gibbs energy change for all studied systems, except for the model system $\text{HO}_2\bullet + \text{HO}_2\bullet$, for which other reaction channels are in any case known to dominate. We have also demonstrated in our previous research that the alkoxy radical products react readily via hydrogen-shift or recombination reactions, which terminate the radicals and lower the total energies considerably. Furthermore, based on the mechanistic insights gained from our multireference calculations—in particular, the rate-limiting nature of the tetroxide formation step—we were able to estimate bimolecular overall reaction rate coefficients also at the DFT+CCSD(T) level of theory. These were consistent and comparable to experimental data, which further substantiates the studied mechanism.

■ ASSOCIATED CONTENT

SI Supporting Information

The Supporting Information is available free of charge at <https://pubs.acs.org/doi/10.1021/acs.jpca.2c01321>.

Details of orbital rotation method for coupled-cluster calculations, active space generation and orbital visualization, size-consistency analysis of CASSCF and XMC-QDPT2, thermodynamic data for bimolecular reaction rate coefficients and elementary TST rate coefficient calculations, master equation modeled reaction rates, discussion of ASCI-SCF results, reaction coordinate graphs, xyz-coordinates, and total energy of various studied systems (PDF)

■ AUTHOR INFORMATION

Corresponding Authors

Vili-Taneli Salo – Department of Chemistry, Faculty of Science, University of Helsinki, Helsinki FI-00014, Finland; Email: vili-taneli.salo@helsinki.fi

Theo Kurtén – Department of Chemistry, Faculty of Science, University of Helsinki, Helsinki FI-00014, Finland; orcid.org/0000-0002-6416-4931; Email: theo.kurten@helsinki.fi

Authors

Rashid Valiev – Department of Chemistry, Faculty of Science, University of Helsinki, Helsinki FI-00014, Finland; orcid.org/0000-0002-2088-2608

Susi Lehtola – Department of Chemistry, Faculty of Science, University of Helsinki, Helsinki FI-00014, Finland; Molecular Sciences Software Institute, Blacksburg, Virginia 24061, United States; orcid.org/0000-0001-6296-8103

Complete contact information is available at: <https://pubs.acs.org/10.1021/acs.jpca.2c01321>

Author Contributions

The manuscript was written through contributions of all authors. All authors have given approval to the final version of the manuscript.

Notes

The authors declare no competing financial interest.

Data Available: The data underlying this study (output-files of quantum chemical calculations) are openly available in "Supplementary Data for 'Gas-phase Peroxyl Radical Recombination Reactions: A Computational Study of Formation and Decomposition of Tetroxides'" at [10.5281/zenodo.6517406](https://doi.org/10.5281/zenodo.6517406).

ACKNOWLEDGMENTS

This work was funded by the doctoral programme in chemistry and molecular sciences (CHEMS) in the university of Helsinki. We want to acknowledge CSC – IT Center for Science, Finland, for computational resources, and the Academy of Finland as well as the Jane and Aatos Erkkö Foundation (JAES) for funding. Lastly, we wish to thank Galib Hasan, Thomas Golin Almeida, Christopher David Daub, Siddharth Iyer, and Noora Hyttinen.

REFERENCES

- (1) Lightfoot, P. D.; Cox, R. A.; Crowley, J. N.; Destriau, M.; Hayman, G. D.; Jenkin, M. E.; Moortgat, G. K.; Zabel, F. Organic Peroxy Radicals: Kinetics, Spectroscopy and Tropospheric Chemistry. *Atmospheric Environment. Part A. General Topics* **1992**, *26*, 1805–1961.
- (2) Vereecken, L.; Francisco, J. S. Theoretical Studies of Atmospheric Reaction Mechanisms in the Troposphere. *Chem. Soc. Rev.* **2012**, *41*, 6259–6293.
- (3) Kroll, J. H.; Seinfeld, J. H. Chemistry of Secondary Organic Aerosol: Formation and Evolution of Low-volatility Organics in the Atmosphere. *Atmos. Environ.* **2008**, *42*, 3593–3624.
- (4) Pandis, S. N.; Harley, R. A.; Cass, G. R.; Seinfeld, J. H. Secondary Organic Aerosol Formation and Transport. *Atmospheric Environment. Part A. General Topics* **1992**, *26*, 2269–2282.
- (5) Mauderly, J.; Chow, J. Health Effects of Organic Aerosols. *Inhalation Toxicology* **2008**, *20*, 257–88.
- (6) Zhang, R.; Wang, G.; Guo, S.; Zamora, M. L.; Ying, Q.; Lin, Y.; Wang, W.; Hu, M.; Wang, Y. Formation of Urban Fine Particulate Matter. *Chem. Rev.* **2015**, *115*, 3803–3855.
- (7) Shrivastava, M.; Cappa, C.; Fan, J.; Goldstein, A.; Guenther, A.; Jimenez, J.; Kuang, C.; Laskin, A.; Martin, S.; Ng, N.; et al. Recent Advances in Understanding Secondary Organic Aerosol: Implications for Global Climate Forcing. *Reviews of Geophysics* **2017**, *55*, 509–559.
- (8) Fall, R. Chapter 2 - Biogenic Emissions of Volatile Organic Compounds from Higher Plants. In *Reactive Hydrocarbons in the Atmosphere*, Hewitt, C. N., Ed.; Academic Press: San Diego, 1999; pp 41–96.
- (9) Friedrich, R.; Obermeier, A. Chapter 1 - Anthropogenic Emissions of Volatile Organic Compounds. In *Reactive Hydrocarbons in the Atmosphere*, Hewitt, C. N., Ed.; Academic Press: San Diego, 1999; pp 1–39.
- (10) Bridgman, S. D.; Cadillo-Quiroz, H.; Keller, J. K.; Zhuang, Q. Methane Emissions from Wetlands: Biogeochemical, Microbial, and Modeling Perspectives from Local to Global Scales. *Global Change Biology* **2013**, *19*, 1325–1346.
- (11) Calogirou, A.; Larsen, B. R.; Kotzias, D. Gas-phase Terpene Oxidation Products: A Review. *Atmos. Environ.* **1999**, *33*, 1423–1439.
- (12) Simic, M. G. Free Radical Mechanisms in Autoxidation Processes. *J. Chem. Educ.* **1981**, *58*, 125.
- (13) Bianchi, F.; Kurtén, T.; Riva, M.; Mohr, C.; Rissanen, M. P.; Roldin, P.; Berndt, T.; Crounse, J. D.; Wennberg, P. O.; Mentel, T. F.; et al. Highly Oxygenated Organic Molecules (HOM) from Gas-Phase Autoxidation Involving Peroxy Radicals: A Key Contributor to Atmospheric Aerosol. *Chem. Rev.* **2019**, *119*, 3472–3509.
- (14) Crounse, J. D.; Nielsen, L. B.; Jørgensen, S.; Kjaergaard, H. G.; Wennberg, P. O. Autoxidation of Organic Compounds in the Atmosphere. *J. Phys. Chem. Lett.* **2013**, *4*, 3513–3520.
- (15) Atkinson, R. Atmospheric Chemistry of VOCs and NO_x. *Atmos. Environ.* **2000**, *34*, 2063–2101.
- (16) Villenave, E.; Lesclaux, R. Kinetics of the Cross Reactions of CH₃O₂ and C₂H₅O₂ Radicals with Selected Peroxy Radicals. *J. Phys. Chem.* **1996**, *100*, 14372–14382.
- (17) Orlando, J. J.; Tyndall, G. S. Laboratory Studies of Organic Peroxy Radical Chemistry: An Overview with Emphasis on Recent Issues of Atmospheric Significance. *Chem. Soc. Rev.* **2012**, *41*, 6294–6317.
- (18) Russell, G. A. Deuterium-isotope Effects in the Autoxidation of Alkyl Hydrocarbons. Mechanism of the Interaction of Peroxy Radicals¹. *J. Am. Chem. Soc.* **1957**, *79*, 3871–3877.
- (19) Bartlett, P. D.; Traylor, T. G. Oxygen-18 Tracer Studies of Alkylperoxy Radicals. I. The Cumylperoxy Radical and Chain Termination in the Autoxidation of Cumene. *J. Am. Chem. Soc.* **1963**, *85*, 2407–2410.
- (20) Bartlett, P. D.; Guaraldi, G. Di-*t*-butyl Trioxide and Di-*t*-butyl Tetroxide. *J. Am. Chem. Soc.* **1967**, *89*, 4799–4801.
- (21) Adamic, K.; Howard, J. A.; Ingold, K. U. Di-*t*-alkyl Tetroxides. *Journal of the Chemical Society D: Chemical Communications* **1969**, 505–506.
- (22) Bennett, J. E.; Brown, D. M.; Mile, B. The Equilibrium between Tertiary Alkylperoxy-radicals and Tetroxide Molecules. *Journal of the Chemical Society D: Chemical Communications* **1969**, 504–505.
- (23) Kirsch, L. J.; Parkes, D. A.; Waddington, D. J.; Woolley, A. Reactions of Oxygenated Radicals in the Gas Phase. Part 6.—Reactions of Isopropylperoxy and Isopropoxy Radicals. *Journal of the Chemical Society, Faraday Transactions 1: Physical Chemistry in Condensed Phases* **1979**, *75*, 2678–2687.
- (24) Cowley, L. T.; Waddington, D. J.; Wooley, A. Reactions of Oxygenated Radicals in the Gas Phase. Part 9.—Self-reactions of Isopropylperoxy Radicals. *Journal of the Chemical Society, Faraday Transactions 1: Physical Chemistry in Condensed Phases* **1982**, *78*, 2535–2546.
- (25) Tyndall, G. S.; Cox, R. A.; Granier, C.; Lesclaux, R.; Moortgat, G. K.; Pilling, M. J.; Ravishankara, A. R.; Wallington, T. J. Atmospheric Chemistry of Small Organic Peroxy Radicals. *Journal of Geophysical Research: Atmospheres* **2001**, *106*, 12157–12182.
- (26) Nangia, P. S.; Benson, S. W. The Kinetics of the Interaction of Peroxy Radicals. II. Primary and Secondary Alkyl Peroxy. *International Journal of Chemical Kinetics* **1980**, *12*, 43–53.
- (27) Howard, J. A.; Bennett, J. E. The Self-Reaction of *sec*-Alkylperoxy Radicals: A Kinetic Electron Spin Resonance Study. *Can. J. Chem.* **1972**, *50*, 2374–2377.
- (28) Zhang, P.; Wang, W.; Zhang, T.; Chen, L.; Du, Y.; Li, C.; Lü, J. Theoretical Study on the Mechanism and Kinetics for the Self-Reaction of C₂H₅O₂ Radicals. *J. Phys. Chem. A* **2012**, *116*, 4610–4620.
- (29) Liang, Y.-N.; Li, J.; Wang, Q.-D.; Wang, F.; Li, X.-Y. Computational Study of the Reaction Mechanism of the Methylperoxy Self-Reaction. *J. Phys. Chem. A* **2011**, *115*, 13534–13541.
- (30) Ghigo, G.; Maranzana, A.; Tonachini, G. Combustion and Atmospheric Oxidation of Hydrocarbons: Theoretical Study of the Methyl Peroxyl Self-reaction. *J. Chem. Phys.* **2003**, *118*, 10575–10583.
- (31) Roos, B. O.; Taylor, P. R.; Sigbahn, P. E. M. A Complete Active Space SCF Method (CASCF) Using a Density Matrix Formulated Super-CI Approach. *Chem. Phys.* **1980**, *48*, 157–173.
- (32) Valiev, R. R.; Hasan, G.; Salo, V.-T.; Kubečka, J.; Kurten, T. Intersystem Crossings Drive Atmospheric Gas-Phase Dimer Formation. *J. Phys. Chem. A* **2019**, *123*, 6596–6604.
- (33) Hasan, G.; Salo, V.-T.; Valiev, R. R.; Kubečka, J.; Kurtén, T. Comparing Reaction Routes for ³(RO···OR') Intermediates Formed in Peroxy Radical Self- and Cross-Reactions. *J. Phys. Chem. A* **2020**, *124*, 8305–8320.

- (34) *Spartan 16*; Wavefunction, Inc., Irvine, California, 2016.
- (35) Halgren, T. A. Merck Molecular Force Field. I. Basis, Form, Scope, Parameterization, and Performance of MMFF94. *J. Comput. Chem.* **1996**, *17*, 490–519.
- (36) Stephens, P. J.; Devlin, F. J.; Chabalowski, C. F.; Frisch, M. J. Ab Initio Calculation of Vibrational Absorption and Circular Dichroism Spectra Using Density Functional Force Fields. *J. Phys. Chem.* **1994**, *98*, 11623–11627.
- (37) Clark, T.; Chandrasekhar, J.; Spitznagel, G. W.; Schleyer, P. V. R. Efficient Diffuse Function-augmented Basis Sets for Anion Calculations. III. The 3-21+G Basis Set for First-row Elements, Li–F. *J. Comput. Chem.* **1983**, *4*, 294–301.
- (38) Ditchfield, R.; Hehre, W. J.; Pople, J. A. Self-Consistent Molecular-Orbital Methods. IX. An Extended Gaussian-Type Basis for Molecular-Orbital Studies of Organic Molecules. *J. Chem. Phys.* **1971**, *54*, 724–728.
- (39) Hariharan, P. C.; Pople, J. A. The Influence of Polarization Functions on Molecular Orbital Hydrogenation Energies. *Theoretica chimica acta* **1973**, *28*, 213–222.
- (40) Hehre, W. J.; Ditchfield, R.; Pople, J. A. Self-Consistent Molecular Orbital Methods. XII. Further Extensions of Gaussian-Type Basis Sets for Use in Molecular Orbital Studies of Organic Molecules. *J. Chem. Phys.* **1972**, *56*, 2257–2261.
- (41) Becke, A. D. A New Mixing of Hartree–Fock and Local Density-functional Theories. *J. Chem. Phys.* **1993**, *98*, 1372–1377.
- (42) Lee, C.; Yang, W.; Parr, R. G. Development of the Colle-Salvetti Correlation-energy Formula into a Functional of the Electron Density. *Phys. Rev. B* **1988**, *37*, 785–789.
- (43) Frisch, M. J.; Trucks, G. W.; Schlegel, H. B.; Scuseria, G. E.; Robb, M. A.; Cheeseman, J. R.; Scalmani, G.; Barone, V.; Petersson, G. A.; Nakatsuji, H., et al. *Gaussian 16 Rev. C.01*; Gaussian: Wallingford, CT, 2016.
- (44) Krishnan, R.; Binkley, J. S.; Seeger, R.; Pople, J. A. Self-consistent Molecular Orbital Methods. XX. A Basis Set for Correlated Wave Functions. *J. Chem. Phys.* **1980**, *72*, 650–654.
- (45) Chai, J.-D.; Head-Gordon, M. Long-range Corrected Hybrid Density Functionals with Damped Atom–atom Dispersion Corrections. *Phys. Chem. Chem. Phys.* **2008**, *10*, 6615–6620.
- (46) Kendall, R. A.; Dunning, T. H.; Harrison, R. J. Electron Affinities of the First-row Atoms Revisited. Systematic Basis Sets and Wave Functions. *J. Chem. Phys.* **1992**, *96*, 6796–6806.
- (47) Dunning, T. H. Gaussian Basis Sets for Use in Correlated Molecular Calculations. I. The Atoms Boron Through Neon and Hydrogen. *J. Chem. Phys.* **1989**, *90*, 1007.
- (48) Møller, K. H.; Otkjær, R. V.; Hyttinen, N.; Kurtén, T.; Kjaergaard, H. G. Cost-Effective Implementation of Multiconformer Transition State Theory for Peroxy Radical Hydrogen Shift Reactions. *J. Phys. Chem. A* **2016**, *120*, 10072–10087.
- (49) Granovsky, A. A. *Firefly*, ver. 8.2.0.
- (50) Schmidt, M. W.; Baldridge, K. K.; Boatz, J. A.; Elbert, S. T.; Gordon, M. S.; Jensen, J. H.; Koseki, S.; Matsunaga, N.; Nguyen, K. A.; Su, S.; et al. General Atomic and Molecular Electronic Structure System. *J. Comput. Chem.* **1993**, *14*, 1347–1363.
- (51) Sayvetz, A. The Kinetic Energy of Polyatomic Molecules. *J. Chem. Phys.* **1939**, *7*, 383–389.
- (52) Granovsky, A. A. Extended Multi-Configuration Quasi-degenerate Perturbation Theory: The New Approach to Multi-state Multi-reference Perturbation Theory. *J. Chem. Phys.* **2011**, *134*, 214113.
- (53) Tubman, N. M.; Lee, J.; Takeshita, T. Y.; Head-Gordon, M.; Whaley, K. B. A Deterministic Alternative to the Full Configuration Interaction Quantum Monte Carlo Method. *J. Chem. Phys.* **2016**, *145*, 044112.
- (54) Levine, D. S.; Hait, D.; Tubman, N. M.; Lehtola, S.; Whaley, K. B.; Head-Gordon, M. CASSCF with Extremely Large Active Spaces Using the Adaptive Sampling Configuration Interaction Method. *J. Chem. Theory Comput.* **2020**, *16*, 2340–2354.
- (55) Epifanovsky, E.; Gilbert, A. T. B.; Feng, X.; Lee, J.; Mao, Y.; Mardirossian, N.; Pokhilko, P.; White, A. F.; Coons, M. P.; Dempwolff, A. L.; et al. Software for the Frontiers of Quantum Chemistry: An Overview of Developments in the Q-Chem 5 Package. *J. Chem. Phys.* **2021**, *155*, 084801.
- (56) Peterson, K. A.; Adler, T. B.; Werner, H.-J. Systematically Convergent Basis Sets for Explicitly Correlated Wavefunctions: The Atoms H, He, B–Ne, and Al–Ar. *J. Chem. Phys.* **2008**, *128*, 084102.
- (57) Adler, T. B.; Knizia, G.; Werner, H.-J. A Simple and Efficient CCSD(T)-F12 Approximation. *J. Chem. Phys.* **2007**, *127*, 221106.
- (58) Werner, H.-J.; Knowles, P. J.; Knizia, G.; Manby, F. R.; Schütz, M. Molpro: A General-purpose Quantum Chemistry Program Package. *WIREs Computational Molecular Science* **2012**, *2*, 242–253.
- (59) Pavošević, F.; Peng, C.; Pinski, P.; Riplinger, C.; Neese, F.; Valeev, E. F. SparseMaps—A Systematic Infrastructure for Reduced Scaling Electronic Structure Methods. V. Linear Scaling Explicitly Correlated Coupled-cluster Method with Pair Natural Orbitals. *J. Chem. Phys.* **2017**, *146*, 174108.
- (60) Neese, F. The ORCA Program System. *WIREs Computational Molecular Science* **2012**, *2*, 73–78.
- (61) Neese, F. Software Update: The ORCA Program System, Version 4.0. *WIREs Computational Molecular Science* **2018**, *8*, e1327.
- (62) Vaucher, A. C.; Reiher, M. Steering Orbital Optimization out of Local Minima and Saddle Points Toward Lower Energy. *J. Chem. Theory Comput.* **2017**, *13*, 1219–1228.
- (63) Seeger, R.; Pople, J. A. Self-consistent Molecular Orbital Methods. XVIII. Constraints and Stability in Hartree–Fock Theory. *J. Chem. Phys.* **1977**, *66*, 3045–3050.
- (64) Karton, A.; Martin, J. M. L. Explicitly Correlated Wn Theory: W1-F12 and W2-F12. *J. Chem. Phys.* **2012**, *136*, 124114.
- (65) Johnson, R. D., III *NIST 101. Computational Chemistry Comparison and Benchmark Database*; 2020. DOI: 10.18434/T47C7Z.
- (66) Hapka, M.; Krzemińska, A.; Pernal, K. How Much Dispersion Energy Is Included in the Multiconfigurational Interaction Energy? *J. Chem. Theory Comput.* **2020**, *16*, 6280–6293.
- (67) Georgievskii, Y.; Klippenstein, S. J. Long-range Transition State Theory. *J. Chem. Phys.* **2005**, *122*, 194103.
- (68) Glowacki, D. R.; Liang, C.-H.; Morley, C.; Pilling, M. J.; Robertson, S. H. MESMER: An Open-Source Master Equation Solver for Multi-Energy Well Reactions. *J. Phys. Chem. A* **2012**, *116*, 9545–9560.
- (69) Daub, C. D.; Valiev, R.; Salo, V.-T.; Zakai, I.; Gerber, R. B.; Kurtén, T., Simulated Pre-reactive Complex Association Lifetimes Explain Trends in Experimental Reaction Rates for Peroxy Radical Recombinations with Submerged Barriers. Unpublished manuscript, **2022**.
- (70) Daub, C. D.; Zakai, I.; Valiev, R.; Salo, V.-T.; Gerber, R. B.; Kurtén, T. Energy Transfer, Pre-reactive Complex Formation and Recombination Reactions During the Collision of Peroxy Radicals. *Phys. Chem. Chem. Phys.* **2022**, *24*, 10033.